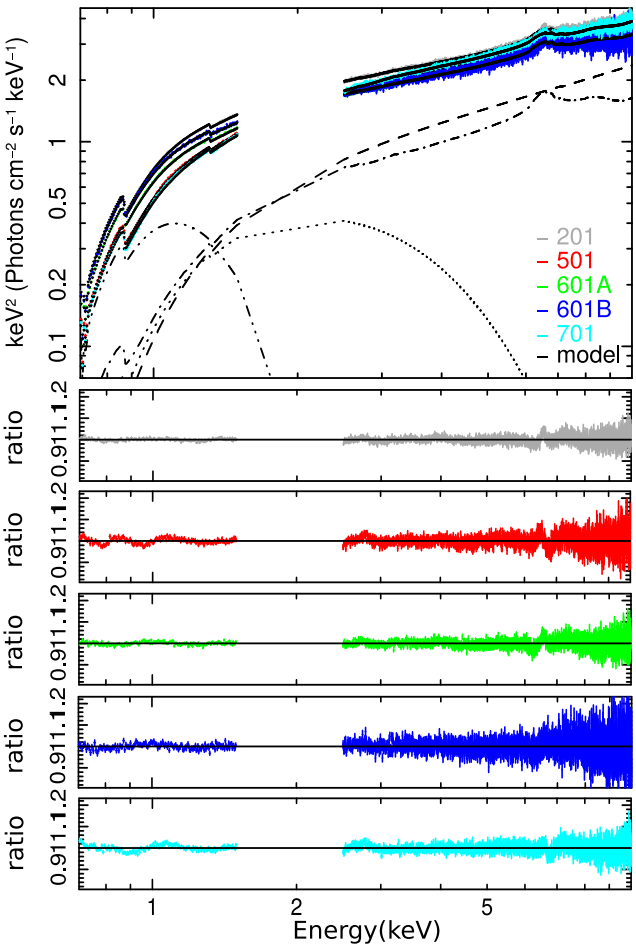

Figure 4. The best-fit models from the joint fit of the NWA time-averaged spectra of all the observations (observation 601 is divided in two due to a gap in the data). The best-fit model (`Tbnew × [diskbb + nthComp + relxillCp]`) is overplotted in black (solid curve) for each observation. For clarity, the single components of the model are reported only for observation 201: triple-dot-dashes correspond to the disc blackbody (`diskbb`), dots to the soft excess (`nthComp`), dashes to the hard Comptonisation component (`relxillCp` Comptonised part only) and dot-dashes to its reflection with the disc (`relxillCp` reflection part only). There are large instrumental residuals in the energy range 1.5–2.5 keV, so this range is excluded from the fit. The bottom panels show the ratios of the data to the best-fit model for each spectrum separately.

We find that the intrinsic coherence of the Total dataset changes significantly among the different observations (ranging between $\sim$ 0.6–0.9), and we ascribe this behaviour to the presence of the wind. Indeed, for this dataset, the lowest values of intrinsic coherence are registered during the observations characterized by stronger absorption (observation 201 and 701). On the other hand, the intrinsic coherence of the NWA dataset is high ($\sim$ 0.95) and consistent with being constant among observations, as commonly observed (e.g. Nowak et al. 1999; Pottschmidt et al. 2003; Grinberg et al. 2014). In other words, when considering the "bare" emission from the X-ray source, there are no indications of significant changes of coherence between variability in the two energy bands.

4.2 Lag-frequency spectra

We then computed the frequency-dependent time lags between the same soft and hard energy bands used to compute the intrinsic coherence in Sect. 4.1. The time lags were estimated as $\tau(\nu) = \phi(\nu)/2\pi\nu$, where $\phi(\nu)$ is the phase lag of the average (over the different light curve segments of a single observation) cross-spectrum. Results are shown in Fig. 6, for both the Total (blue) and NWA (green) datasets of each observation.

We observe that the amplitude of the lag is positive at all frequencies, indicating that rapid variability in the 2–10 keV energy band is delayed with respect to the 0.3–1 keV band. Interestingly, there is no evidence of a thermal reverberation lag in the 1–10 Hz range (which would manifest as a negative lag representing a delay of the disc-dominated, 0.3–1 keV band with respect to the Comptonisation-dominated 2–10 keV band). While hard lags are commonly observed in BHXRBs (e.g. Nowak et al. 1999; Uttley et al. 2011; De Marco et al. 2015), we note that the wind affects their amplitude at low frequencies. Indeed, during observations 201 and (to a lesser degree) 701, the Total datasets display slightly shorter low frequency hard lags than during the other observations. We further investigated this issue in Sect. 4.3 for the most absorbed observation. After correcting for the effects of wind-absorption (NWA dataset in Fig. 6), the amplitude of the low frequency hard lags in observations 201 and 701 increases, becoming consistent with the lags measured in the other observations[4].

4.3 The X-ray spectral-timing properties of the stellar wind

Given the observed differences between the Total and the NWA datasets, we investigated in more detail the spectral-timing signatures of the X-ray variability induced by the stellar wind. We did so by analysing time intervals dominated by wind absorption, thus corresponding to the deeper phases of each X-ray dipping event (Fig. 1). To this aim we focused on observation 201 (which covers the first passage at superior conjunction), as this displays the largest number of absorption dips in the light curve and the densest track in the colour-colour diagram of the source (Figs. 1 and 2). We first studied the dependence of the measured fractional rms on the amount of absorbing material along the line of sight. We selected 8 different regions of soft and hard colours which, for a given covering factor (Appendix A), would correspond to increasing values (from A to H in Fig. 7) of the column density $N_{H,w}$. Using the same procedure as in Sect. 3, we computed the average PSD of the data within each selected regions. The PSDs are extracted in the soft, intermediate and hard energy bands used in Sect. 2.1, and are displayed in Fig. 8. At both low and high frequencies we can observe significant differences as a function of the amount of intervening gas. In particular, we register a gradual increase of low frequency variability and a decrease of high frequency variability power. Above a certain value of $N_{H,w}$ (regions D to H of the colour-colour diagram), in the soft and in the intermediate bands (Fig. 8, upper and middle panel) the variability power starts to be suppressed also at lower frequencies. In other words, at the bottom of the dip, soft band variability is significantly damped on all sampled timescales, while this suppression appears to occur only above an increasingly higher frequency as the energy increases.

In order to better visualise these trends, we integrated the

[4] The shorter low frequency hard lags for observation 701 could be related to residual wind absorption as mentioned in Sect. 3

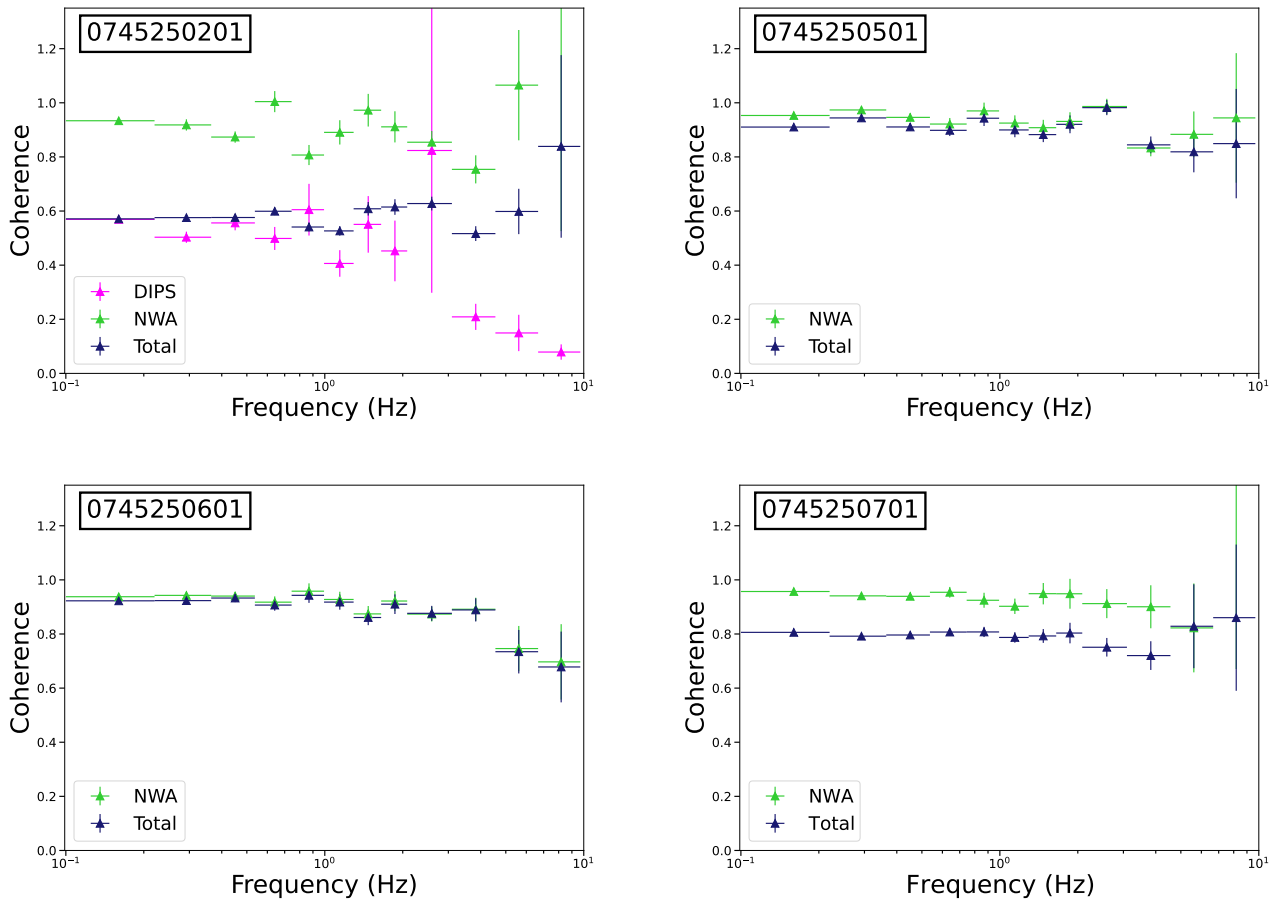

Figure 5. Intrinsic coherence between the 0.3–1 keV and the 2–10 keV energy bands for the Total (blue) and NWA (green) datasets. For observation 201, the DIPS dataset (hard colour $\leqslant 0.8$) is shown in magenta

PSDs over the 0.16–0.6 Hz and the 2–5 Hz frequency intervals. The resulting fractional rms in each frequency range is plotted separately (see Fig. 9) for each energy band as a function of the selected region of the colour-colour diagram.

The 0.16–0.6 Hz fractional rms initially increases up to $\sim$ 23–25 percent. Then it starts decreasing, reaching values of $\sim$ 10–17 percent. This change in the overall trend occurs in regions of the colour-colour diagram characterised by higher values of $N_{H,w}$. In the softest band the trend reversal occurs earlier in the colour-colour diagram track (i.e. at higher values of the hard colour) than seen in higher energy bands. At soft energies, the most affected by absorption, we also register the highest/lowest values of maximum/minimum fractional rms. While the hardest energy band does not show evidence of a drop of 0.16–0.6 Hz fractional rms, an increasing trend can still be clearly observed, suggesting absorption affects also this region of the spectrum.

On the other hand, the 2–5 Hz fractional rms steadily decreases (from $\sim$ 15 to $\sim$ 12 percent) in all bands, eventually reaching a plateau (between regions D and H).

The increase of fractional rms, observed at low frequencies in some regions of the colour-colour diagram and at different levels for different energy bands, can be explained in terms of variations of the column density of the absorbing gas crossing the line of sight to the X-ray source. However, the suppression of variability that occurs in the most absorbed phases/energy bands, and at the highest sampled frequencies requires the presence of additional scattering components (see discussion in Sect. 5).

Finally, we measured again the coherence and the lags between the 0.3–1 keV and the 2–10 keV energy bands (as in Sects. 4.1 and 4.2), this time using a dataset which selects only intervals strongly affected by the wind (i.e. with a hard colour $\leqslant 0.8$). This dataset (hereafter referred to as "DIPS") roughly corresponds to the regions D to H in Fig. 7. The results are overplotted in Figs. 5 and 6. A comparison with the Total and NWA datasets clearly demonstrates that wind absorption is the main cause of the lower coherence and shorter hard lags measured in the Total dataset during each passage at superior conjunction. Indeed, the X-ray variability associated with the stellar wind is characterised by a low intrinsic coherence ($\lesssim 0.5$, and dropping to zero above 2 Hz) and a negative (soft) lag of a few tens of msec.

5 DISCUSSION

Detailed studies of the stellar wind in Cyg X-1 have been mostly focused on characterizing the way the wind influences the spectral properties of the system, and generally limited to $E \gtrsim 1$ keV (e.g. Grinberg et al. 2015; Hirsch et al. 2019). On the other hand, studies

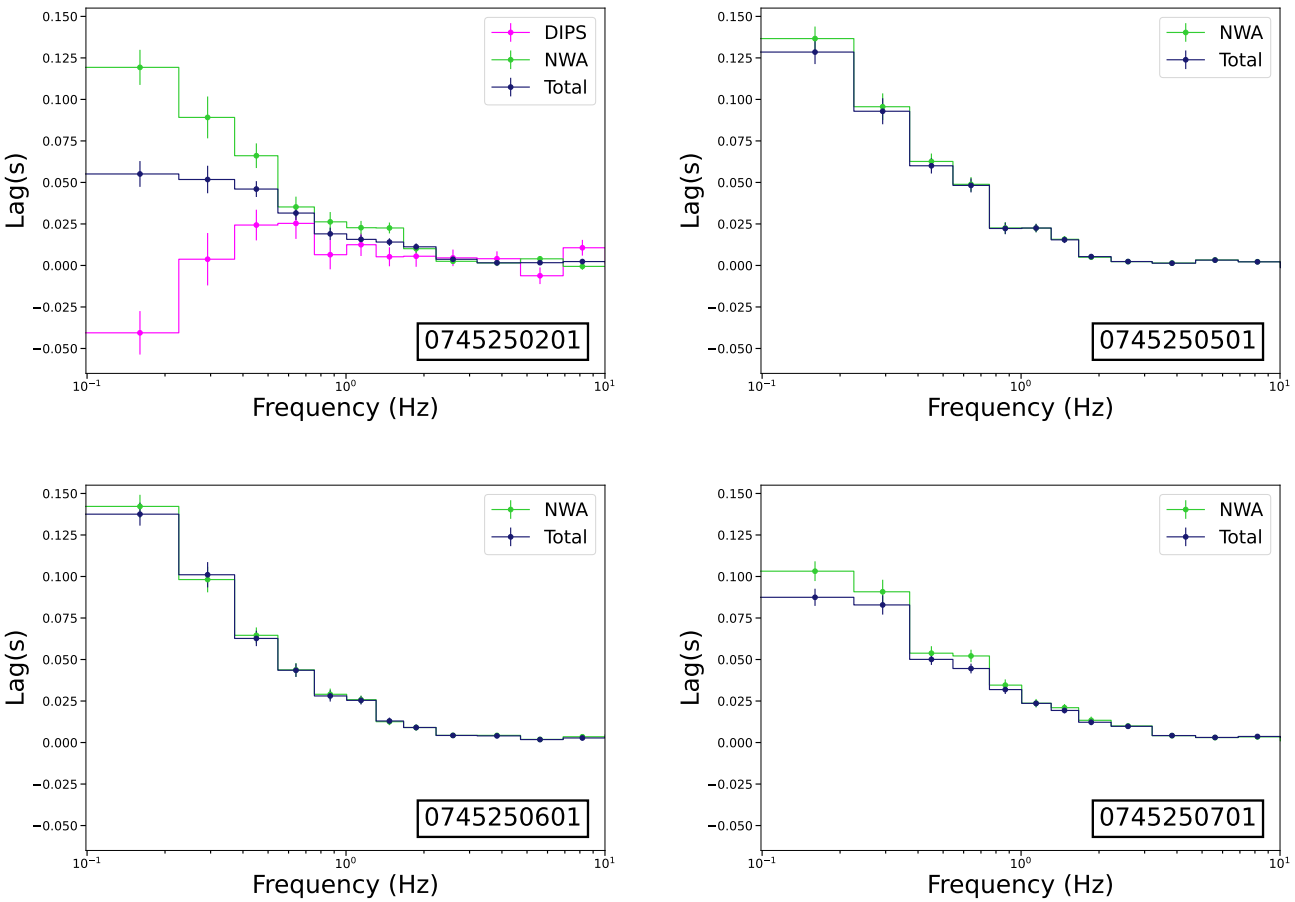

Figure 6. Lag-frequency spectra between the 2–10 keV and the 0.3–1 keV energy band for Total (blue) and NWA (green) datasets. In magenta, the DIPS dataset (with a hard colour $\leqslant 0.8$) for observation 201.

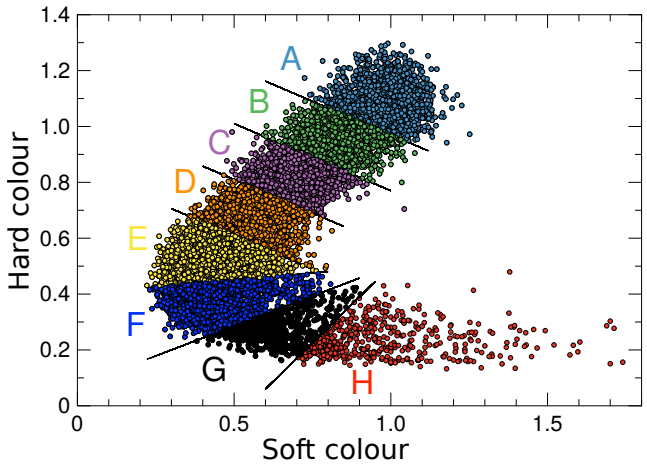

Figure 7. The colour-colour diagram of observation 201 showing the regions selected for the study of the PSD as a function of the amount of absorption. From A to H the different regions correspond (for a constant covering factor) to an increasing value of $N_{H,w}$.

of the X-ray timing properties of Cyg X-1 have been mostly focused on the X-ray source, neglecting the effects of the wind (e.g. Pottschmidt et al. 2003; Axelsson & Done 2018; Mahmoud & Done 2018a,b).

In this paper we found that the presence of a stellar wind significantly affects the X-ray variability power of the source, as well as the amount of coherence and the amplitude of the lags between variable emission in the soft (0.3–1 keV) and hard (2–10 keV) energy bands. The observed behaviour changes significantly as a function of the orbital phase, due to the orbital modulation of wind absorption.

5.1 Effects of the wind on the X-ray variability power

We found that the stellar wind influences the observed X-ray variability power of the source in a complex way, that depends on both energy and timescale (Sects. 3 and 4.3). These results are discussed below considering the low and high frequency behaviour separately.

5.1.1 X-ray variability at low frequencies ($\lesssim$ 1 Hz)

The variable X-ray absorption associated with the stellar wind has the effect of increasing the long timescale/low frequency fractional rms of the source (Figs. 3, 8, and red markers in Fig. 9). This wind-induced, excess X-ray variability is observed in all the energy bands

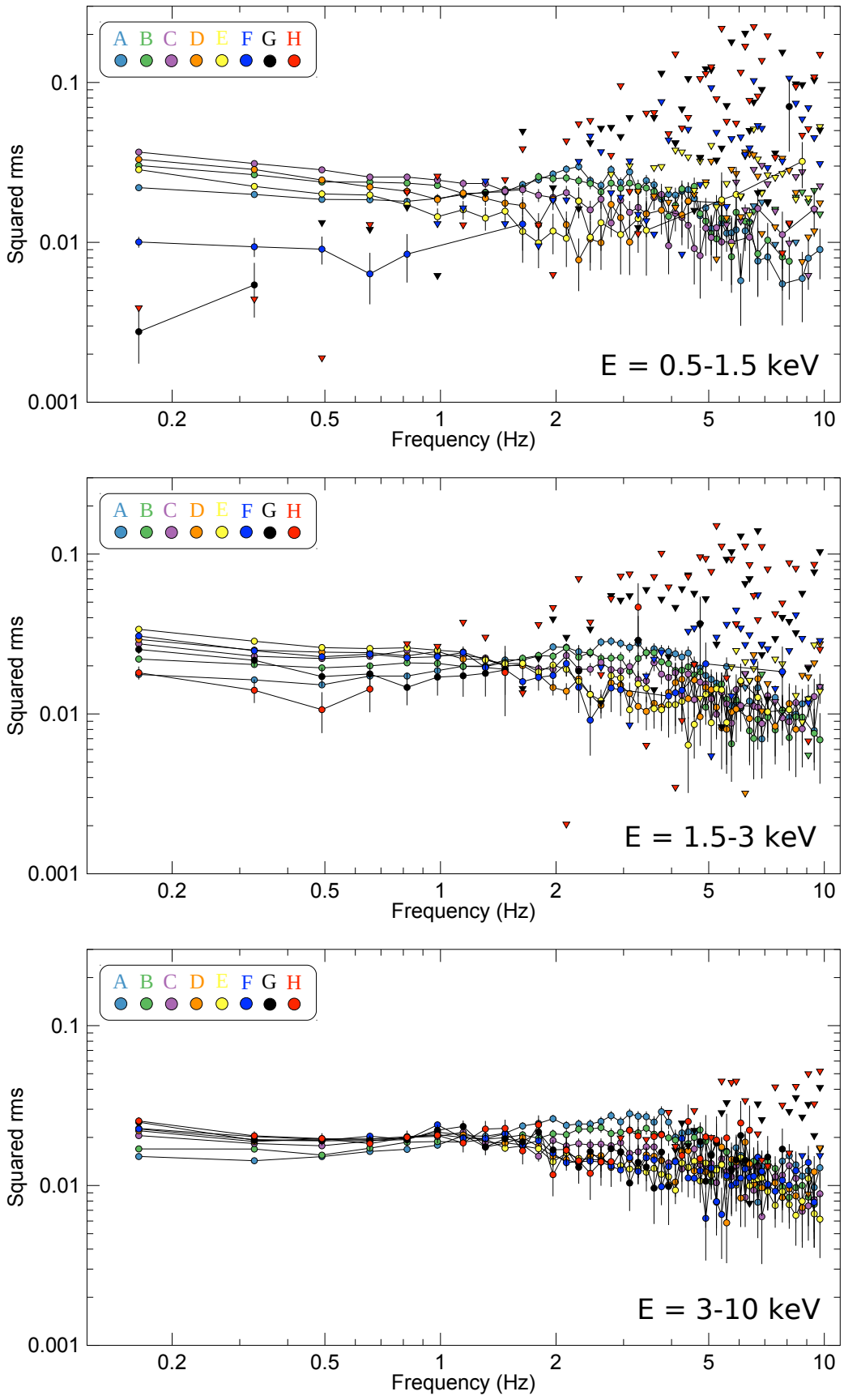

Figure 8. PSDs for the selected regions in Fig. 7 in the soft (0.5–1.5 keV, upper panel), intermediate (1.5–3 keV, middle panel) and hard (3–10 keV, lower panel) bands. The triangles represent upper limits (at 3σ confidence level).

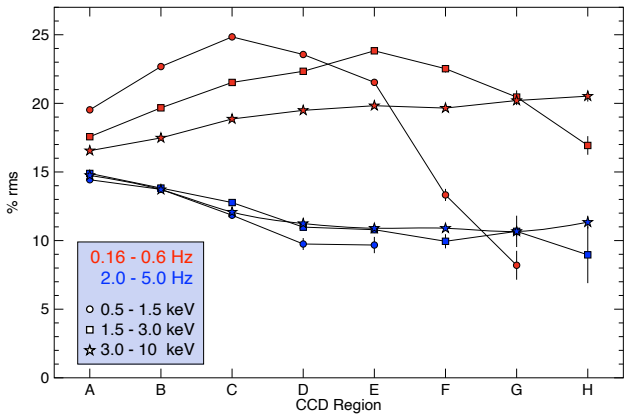

Figure 9. Fractional rms as a function of increasing wind absorption (from region A to region H).

considered, including the highest energies (3–10 keV), in line with spectral studies that showed that the stellar wind can modify the broad band continuum up to very high energies (∼ 10 keV, e.g. Grinberg et al. 2015).

By considering a clumpy wind model, Grinberg et al. (2015) investigated the variability induced by clumps of variable size and porosity (a measure of the mean free path among clumps), and constant mass, as they cross our line of sight. The main inferred effect of these transits is an increase of the observed variability power due to the variations of the $N_{H,w}$ of the intervening structured wind. According to this study, excess X-ray variability would be observed only when averaging over timescales sufficiently short so as to catch the passage of a single/small number of clumps (at lower frequencies/longer timescales wind-induced variability would result washed out as a consequence of averaging over a large number of transits). Although this model may represent a simplification of the real conditions, it clearly shows how variations of the $N_{H,w}$ of the wind can produce an increase of variability power as observed in the data analysed here (Figs. 3, 8, and 9). This would imply that the timescales sampled in our study (∼ 1–10 s) are short enough to catch the passage of single clumps. Grinberg et al. (2015) also note that below/above a certain timescale/temporal frequency the wind does not contribute to increase the level of X-ray variability further. This timescale roughly corresponds to the time needed for a typical clump to transit the line of sight, and thus can be used (knowing the wind velocity) to estimate the typical size of the clumps. We can obtain an estimate of the typical size of the clumps responsible for the observed excess variability in Cyg X-1 by considering the maximum frequency, ν_{max}, at which the variability power in the Total PSD is observed to be greater or equal to the variability power in the NWA PSD. Assuming a wind terminal velocity of $v_\infty = 2400$ km s^{-1} (Grinberg et al. 2015), the resulting radial size of the clumps would be of the order of $l \sim 0.5$–$1.5 \times 10^{-4} R_*$ (we note that the larger values of ∼ 0.02–0.2 R_* previously found by Hirsch et al. 2019 are due to the larger minimum timescale sampled in their analysis, i.e. 25.5 s). This range accounts for the different values of ν_{max} observed in the different observations. We note however, that while this represents an order of magnitude estimate, the clumps likely have a broad distribution of sizes. In particular, smaller clumps can give a significant contribution to the observed high frequency X-ray variability.

When considering the most absorbed stages (which correspond to lower values of hard colour in the colour-colour diagram, Fig. 7, and for a given covering factor, to higher $N_{H,w}$, Fig. A), we found that the low-frequency X-ray variability power in softer bands starts to be significantly suppressed (Fig. 9). Large scale reprocessing/fluorescent scattering of soft band photons in the stellar wind is a plausible mechanism to explain the decrease of low frequency variability power during the dips. Indeed, light travel time differences across this extended medium strongly dilute the intrinsic flux variability of the X-ray source. This constant or slowly variable extended emission component from the wind would dominate the soft X-ray band when the direct continuum is highly absorbed, resulting in a net decrease of fractional rms at these energies. We note that a similar effect might be produced by scattering off dust layers in the ISM (known to produce a soft spectrum due to the energy dependence of the dust scattering cross-section, Predehl & Schmitt 1995; Xiang et al. 2011; Ling et al. 2009). However, this seems less plausible given the factor of ∼ 2 decrease in fractional rms observed during the dips in the softest energy band (Fig. 9), which implies quite a large scattering fraction.

5.1.2 *X-ray variability at high frequencies (≳ 1 Hz)*

The observations during passage at superior conjunction (observations 201 and 701) are characterized by a strong suppression of the high frequency variability hump, a characteristic feature in the power spectrum of Cyg X-1. This can be seen by comparing the Total (as well as the DIPS for observation 201) datasets with the NWA datasets (Figs. 3 and B1). Such a suppression is observed at all energies, and according to Fig. 9, it starts occurring at relatively low levels of wind absorption. Nonetheless, this behaviour cannot be ascribed to absorption in the stellar wind, since variable absorption would result in an increase of fractional rms, while constant absorption would equally affect the variable and constant flux components, thus it would not produce any change in the fractional rms.

Here, we consider the possibility that the suppression of the high frequency variability power is due to scattering, thus smearing out the fastest variability, and infer the optical depth of the scattering medium. The timescales affected by scattering will be those shorter than the light crossing time of the scattering medium, thus corresponding to the highest temporal frequencies in the power spectrum. The temporal frequency where this dampening becomes significant is expected to decrease as the optical depth τ_s increases (e.g. Zdziarski et al. 2010).

Such a behaviour has been previously observed in a number of sources (e.g. Belloni et al. 1991; Berger & van der Klis 1994). Interestingly, in the case of the BHXRB Cyg X-3 the analysis of the PSD required the presence of a gas optically thicker than the wind (Zdziarski et al. 2010). Using equation 5 of Zdziarski et al. (2010) we estimate that the drop observed in Cyg X-1 (at $\nu \sim 5$–10 Hz) would require $\tau_s \sim 0.5$–1 for a scattering region of the size of $R \sim 3 \times 10^9$ cm, as inferred for Cyg X-3. The need for such a large τ is also confirmed by the fact that the suppression of high frequency variability in the PSD of observation 201 is still observed at very high energies (see Fig. 10, reporting the PSD of the Total and NWA datasets of observation 201, extracted in the $E = 6$–10 keV energy band). These results support the hypothesis of the presence of an optically thick gas intercepting the line-of-sight to the X-ray source during superior conjunction. However, previous analyses suggest $\tau_w \ll 1$ for the stellar wind in Cyg X-1 (Zdziarski 2012), remarkably lower than required from our estimates. Therefore, as previously seen in Cyg X-3, a gas optically thicker than its stellar wind is needed to explain the drop of high frequency variability seen